

# Renormalization of Majorana bound state decay length in a perpendicular magnetic field

M. P. Nowak<sup>1</sup> and P. Wójcik<sup>2</sup>

<sup>1</sup>*AGH University of Science and Technology, Academic Centre for Materials and Nanotechnology, al. A. Mickiewicza 30, 30-059 Krakow, Poland*

<sup>2</sup>*AGH University of Science and Technology, Faculty of Physics and Applied Computer Science, al. A. Mickiewicza 30, 30-059 Krakow, Poland*  
(Dated: April 4, 2025)

Orbital effects of a magnetic field in a proximitized semiconductor nanowire are studied in the context of the spatial extent of Majorana bound states. We develop analytical model that explains the impact of concurring effects of paramagnetic coupling of the nanowire bands via the kinetic energy operator and spin-orbit coupling on the Majorana modes. We find, that the perpendicular field, so far considered as detrimental to the Majorana fermion formation, is in fact helpful in establishing the topological zero-energy-modes in a finite system due to significant decrease of the Majorana decay length.

Topological superconductivity created by a combination of the spin-orbit (SO) coupling and the Zeeman effect in a low-dimensional semiconductor-superconductor heterostructures [1, 2] is foreseen as prospective in the quantum computation that exploits manipulation of Majorana bound states (MBSs) [3]. The elementary braiding operation of Majoranas requires at least a three terminal junction. In the pursuit of topological quantum gates creation [4–6] multiterminal networks of MBSs are realized experimentally in a form of nanowire crosses [7, 8] and hashtags [9]. In those structures orientation of the magnetic field perpendicular to the substrate is preferable as it allows to induce the topological phase in all the nanowire branches owing to perpendicular orientation of the field with respect to the SO coupling direction.

In the previous experimental research, large in-plane, type-II superconducting electrodes were sputtered after the nanowire deposition on the substrate [10–14], prohibiting application of the perpendicular magnetic field due to the vortex formation in the superconductor slab. This obstacle has been recently overpassed by realization of 2DEG [15] and nanowire [9, 16] hybrid devices in a bottom-up synthesis with a thin type-I superconducting shell. This guarantees a pristine interface between superconductor and semiconductor materials [17], ensures the hard superconducting gap [18] and allows for observation of a long-predicted conductance doubling in a proximitized quantum point contact [19] or  $2e^2/h$  quantization of Majorana modes [20]. Most importantly, the exploitation of the thin superconducting shell enables arbitrary alignment of the magnetic field without destroying the superconductivity and by that opens a wide perspective for the topological quantum gate creation.

Studies that took into account effects of the magnetic field beyond sole-Zeeman-interaction focused on the impact of the field orientation on the phase boundaries [21–23] and painted somewhat discouraging picture of topological phase instability due to the gap closing in tilted magnetic field [21]. It has been shown however that this is

rather an effect of numerical treatment of the vector potential [22], and in fact the topological phase can still exist in perpendicular orientation of the field. In this work, exploiting analytical treatment of the orbital effects of the perpendicular magnetic field we address problem of the real-space extent of Majorana modes, crucial in the light of topological protection of MBSs in a finite system quantum gates.

Very recently O. Dmytruk and J. Klinovaja [24] pointed out that the diamagnetic effect of the magnetic field oriented *along* the radially symmetric nanowire acts as an effective chemical potential that reduces the energy oscillations of the overlapping MBSs. This is true only for the parallel magnetic field orientation when the paramagnetic effect does not couple the orbital and spin degrees of freedom. As we show, in general case when the magnetic field has a component perpendicular to the nanowire axis or, as in our case, it is simply perpendicular to the nanowire, the paramagnetic coupling of modes with different orbital excitation and opposite spin renormalizes not only the chemical potential but also the effective mass and the SO coupling constant. As a result both the diamagnetic and paramagnetic terms in the kinetic energy operator contribute to the decrease of the spatial extent of the Majorana modes. On the other hand the magnetic field entering through momentum operator in the SO coupling Hamiltonian have distinct and detrimental effects on the reduction of the decay length, which is crucial for current generation of devices where SO coupling is particularly strong [25–27]. We find surprising equalization of the above mentioned effects that results in the decay length comparable, but still less than in the case without the orbital effects of the magnetic field.

We start by writing down Bogoliubov-de Gennes Hamiltonian for a proximitized semiconductor nanowire,

$$H = (\hbar^2 \mathbf{k}^2 / 2m^* - \mu) \sigma_0 \tau_z + \Delta \sigma_0 \tau_x + \alpha (\sigma_x k_y - \sigma_y k_x) \tau_z + E_z \sigma_z \tau_0. \quad (1)$$

where  $\alpha$  is the Rashba SO coupling constant,  $E_z =$

$\frac{1}{2}g\mu_B B$  is the Zeeman term,  $B$  is the external magnetic field oriented in the  $z$ -direction, perpendicular to the nanowire plane and  $\Delta$  is the effective induced pairing potential.  $\sigma_i$  and  $\tau_i$  with  $i = x, y, z$  are the Pauli matrices acting on spin- and particle-hole degrees of freedom, respectively. The orbital effects of the magnetic field are included through the canonical momentum,  $\mathbf{k} = -i\nabla + e\mathbf{A}/\hbar \cdot \tau_z$  with the vector-potential in Lorentz gauge  $\mathbf{A} = [-yB, 0, 0]$ .

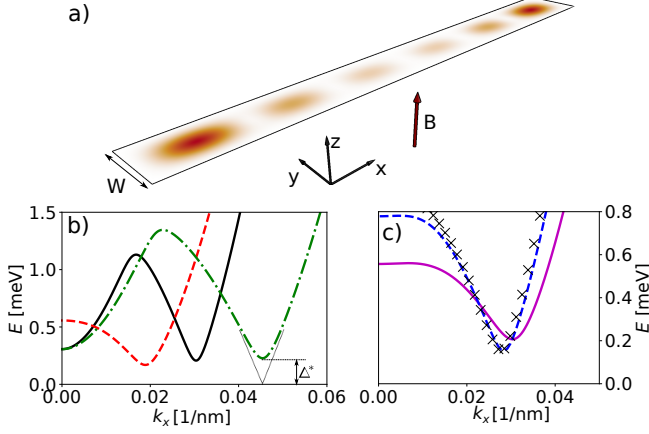


Figure 1. a) Two dimensional crosssection of the proximitized semiconductor nanowire subjected to the magnetic field  $B$  perpendicular to the nanowire axis. The colormap shows an exemplary density distribution of the Majorana bound state. b) Dispersion relations  $E(k)$  obtained in the model of Eq. (9) without the orbital effects (solid black), with the kinetic-paramagnetic term (green dashed) and with the diamagnetic term (red dashed). Their joint effect is presented in panel c) with the pink curve. In c) the blue dashed curve corresponds to the results with the canonical momentum included also in the SO coupling Hamiltonian (SO-paramagnetic term). The black dashes are the results obtained in numerical calculations. Results obtained for  $\mu = 3$  meV,  $\alpha = 50$  meVnm,  $W = 104$  nm,  $B = 0.7$  T.

*Low-energy analysis.* It has been demonstrated that the most convenient situation for realization of MBSs is when a single band of transverse quantization is occupied [23]. We therefore focus on the low electron density regime where the system is tuned such the phase transition occurs due to a single band crossing the Fermi level. Since we are specifically interested in the orbital effects of the magnetic field, for simplicity and without loss of generality, we decouple the spatial degree of freedom collinear with the magnetic field  $z$ -direction and consider the Hamiltonian (1) in the  $x$ - $y$  plane. Figure 1 a) shows the schematic illustration of the considered nanowire oriented along  $x$  (longitudinal) direction with the width  $W$  along  $y$  (transverse) direction.

In contrary to the diamagnetic term ( $\sim y^2 B^2$ ) which solely shifts energies of the electronic states, the paramagnetic effect ( $\sim k_x y B$ ) originating from both the kinetic energy (kinetic-paramagnetic term) and the SO interac-

tion (SO-paramagnetic term), couples the orbital degrees of freedom in the  $y$  direction via the wave vector  $k_x$ . For Majorana fermions in the ground state of transverse quantization, the most significant effect comes from the coupling with the first excited state. For this purpose we write the Hamiltonian (1), in the basis of two lowest eigenstates of infinite quantum well of width  $W$ , centered at  $y = 0$ ,  $\Psi_n(y) = \sqrt{2/W} \sin[n\pi(y + W/2)/W]$ . We obtain

$$H = \begin{pmatrix} H_{11} & H_{12} \\ H_{21} & H_{22} \end{pmatrix}, \quad (2)$$

with

$$H_{11(22)} = H_{1D} + (E_{1(2)} + E_{1(2)}^{\text{dia}})\sigma_0\tau_z, \quad (3)$$

$$H_{12} = H_{21} = \varepsilon_p k_x \sigma_0 \tau_0 + E_p^{SO} \sigma_y \tau_0 + E_{\perp}^{SO} \sigma_x \tau_z, \quad (4)$$

where  $E_n = n^2 \pi^2 \hbar^2 / 2mW^2$  is the energy of orbital excitation in the  $y$ -direction,  $E_n^{\text{dia}} = \langle \Psi_n | y^2 | \Psi_n \rangle e^2 B^2 / 2m$  is the diamagnetic term in the  $n$ 'th subband [with  $\langle \Psi_1 | y^2 | \Psi_1 \rangle = (\pi^2 - 6)W^2 / 12\pi^2$  and  $\langle \Psi_2 | y^2 | \Psi_2 \rangle = (2\pi^2 - 3)W^2 / 24\pi^2$ ] that acts as the extra chemical potential being different for each band. The parameter  $\varepsilon_p = -\langle \Psi_1 | y | \Psi_2 \rangle e B \hbar / m = 16W e B \hbar / m 9\pi^2$  results from the kinetic-paramagnetic effect that due to parity of the transverse modes is non-zero only in the off-diagonal submatrices ( $H_{12}, H_{21}$ ). It mixes the transverse modes with magnitude proportional to the wave-vector  $k_x$ . In Eq. (4),  $E_p^{SO} = \langle \Psi_1 | y | \Psi_2 \rangle \alpha e B / \hbar = -16W \alpha e B / \hbar 9\pi^2$  corresponds to the substitution of the canonical momentum in the SO Hamiltonian that accounts for mixing bands with different transverse excitation and spin along the  $z$ -direction.  $E_{\perp}^{SO} = i\alpha \langle \Psi_1 | \partial / \partial y | \Psi_2 \rangle = i\alpha \frac{8}{3W}$  is a correction due to the transverse part of the Rashba Hamiltonian. In Eq. (3)  $H_{1D}$  is the one-dimensional Hamiltonian along the wire axis

$$H_{1D} = \left( \frac{\hbar^2 k_x^2}{2m^*} - \mu \right) \sigma_0 \tau_z + \Delta \sigma_0 \tau_x - \alpha k_x \sigma_y \tau_z + E_Z \sigma_z \tau_0. \quad (5)$$

In order to solve the problem analytically we use the fact that  $E_2$  is the largest energy in the system. Then, the Hamiltonian  $H_{22}$  can be further simplified to diagonal form neglecting  $\Delta$ ,  $\alpha$ ,  $E_z$  dependencies. As we will see further, this approximation works well and the calculated dispersions  $E(k)$  remain in a good agreement with results obtained from the full numerical diagonalization of the Hamiltonian (2). Using the folding-down transformation [28],  $\mathcal{H}(E) = H_{11} - H_{12}(H_{22} - E)^{-1}H_{21}$ , the  $8 \times 8$  Hamiltonian (2) can be reduced into the  $4 \times 4$  effective Hamiltonian. As we derived, it has the form of  $H_{1D}$  (5) with the renormalized effective mass  $\tilde{m}^*$ , chemical potential  $\tilde{\mu}$  and SO coupling constant  $\tilde{\alpha}$  given by the formulas:

$$\frac{1}{\tilde{m}^*} = \frac{1}{m^*} - \frac{2\varepsilon_p^2}{\hbar^2 E_2}, \quad (6)$$

$$\tilde{\mu} = \mu - E_1 - E_1^{dia} + \frac{(E_p^{SO} - E_{\perp}^{SO})^2}{E_2}, \quad (7)$$

$$\tilde{\alpha} = \alpha + 2 \frac{E_p^{SO} \varepsilon_p}{E_2}. \quad (8)$$

By diagonalization of the renormalized Hamiltonian (5) we find the energies

$$E(k_x) = \pm \sqrt{\tilde{\xi}_1^2 + E_Z^2 + \tilde{\Delta}_{SO}^2 + \Delta^2 \pm 2\sqrt{E_Z^2 \tilde{\xi}_1^2 + \tilde{\Delta}_{SO}^2 \tilde{\xi}_1^2 + \Delta^2 E_Z^2}}, \quad (9)$$

where  $\tilde{\xi}_1 = \hbar^2 k_x^2 / 2\tilde{m}^* - \tilde{\mu}$  and  $\tilde{\Delta}_{SO} = \tilde{\alpha} k_x$ .

The real space extent of MBSs with the wave-function  $\sim e^{-x/\xi}$  is determined by the decay length  $\xi$ . For wires with length  $L \gg \xi$  the modes overlap and their energies are shifted away from zero impairing the topological protection [29]. The localization length  $\xi$  can be determined from the dispersion  $E(k)$  based on the bulk-edge correspondence, which links properties of MBSs for a finite wire with evanescent modes at zero energy calculated for a infinite wire. According to this rule, away from the topological transition,  $\xi$  is characterized by properties of the gapped Dirac cones at  $k \neq 0$  with  $\xi = \hbar\nu/\Delta^*$  in analogy to standard superconducting coherence length, where  $\nu = dE/dk$  is the Fermi velocity and  $\Delta^*$  is the induced gap [see Fig. 1 b)].

In Fig. 1 a) we plot the positive-energy part of the band structure obtained with Eq. (9) without the orbital effects of the magnetic field (black solid curve) and with the kinetic paramagnetic term (green dashed curve) and diamagnetic term (red dashed curve) included. By the analysis of these curves together with the formulas (6), (7) we conclude that the diamagnetic effect lowers the chemical potential, while the paramagnetic effect widens the dispersion relation  $E(k_x)$  due to rescaling of the effective mass. In turn both these effects decrease the slope of the cones at  $k \neq 0$  decreasing the decay length  $\xi$ . Their joint outcome is depicted in Fig. 1 c) with the pink curve. Inspecting Eqs. (7, 8) we note that the paramagnetic term through the SO coupling Hamiltonian *counteracts* the rescaling of the chemical potential and decreases the induced gap due the reduction of the SO coupling constant.

In the limit of small  $\Delta$ ,  $k_x$  and  $\alpha$  one can write an analytical formula for the Majorana decay length [30],

$$\xi \simeq \frac{1}{\tilde{\alpha}\Delta} \sqrt{\left(\frac{\hbar^2}{\tilde{m}^*} \tilde{\mu} + \tilde{\alpha}^2\right)^2 + \left(\frac{\hbar^2}{\tilde{m}^*}\right)^2 (E_Z^2 - \Delta^2 - \tilde{\mu}^2)}. \quad (10)$$

The behavior of the decay length obtained from the above equation reproduces the lengths inferred qualitatively from the band structure. The orbital effects through the kinetic energy operator decrease  $\tilde{\mu}$  and  $1/\tilde{m}^*$  and by that

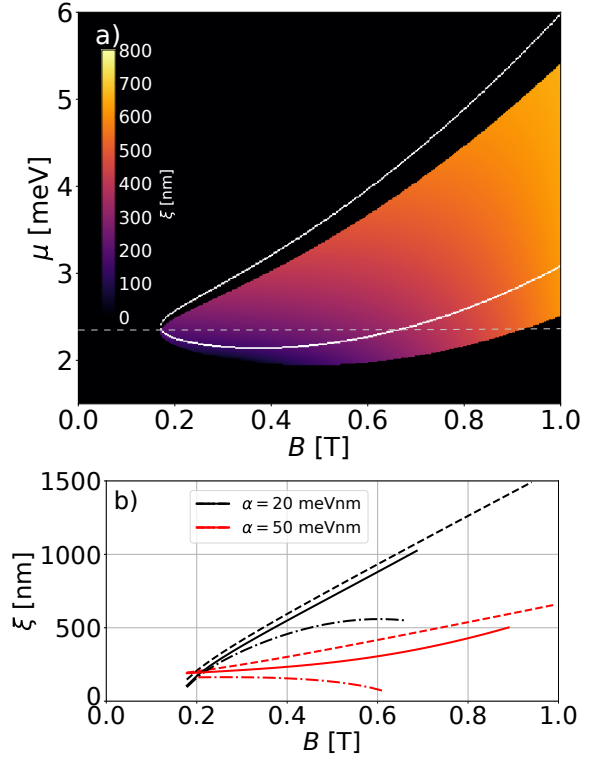


Figure 2. a) Majorana bound state decay length  $\xi$  obtained through Eq. (10). The white contour presents the topological phase boundary  $E_z^2 > \Delta^2 + \tilde{\mu}^2$  when the orbital effects of the magnetic field are included solely through the kinetic energy operator. b) Comparison of the decay length calculated without the orbital effects (dashed curves), with the kinetic-paramagnetic and the diamagnetic contributions included (dot-dashed curves) and with the orbital effects included in both the kinetic energy operator and the SO coupling Hamiltonian (solid curves). Results for  $\alpha = 20$  meVnm are obtained for  $\mu = 2.5$  meV and for  $\alpha = 50$  meVnm for  $\mu = 2.3$  meV – such they both correspond to the  $\mu$  value for which the topological transition occurs at the lowest B – see the dashed line in a).

reduce  $\xi$ . The effects of SO-paramagnetic contribution are more convoluted. Increase of the magnetic field *increases* the effective chemical potential  $\tilde{\mu}$  through  $E_p^{SO}$  term in Eq. (7) counteracting the diamagnetic term contribution. On the same time, the SO coupling constant  $\tilde{\alpha}$  is decreased resulting in overall increase of  $\xi \sim 1/\tilde{\alpha}$ .

We now apply the formula (10) for the case of the state-of-the-art structures made on InSb nanowires covered by an Al shell [8, 9, 20]. We adopt the effective electron mass  $m^* = 0.014$ , induced gap  $\Delta = 250 \mu\text{eV}$  and g-factor  $g = -51$ . The SO interaction strength has been recently probed in various types of measurements and proved to be quite diverse, ranging from  $\alpha \simeq 20$  meVnm in the spin-qubit manipulation experiments [31], through  $\alpha = 50 - 100$  meVnm for the weak antilocalization measurements [25], up to extremely high values  $\alpha = 120$  meVnm or  $\alpha = 266$  meVnm in the transport

experiments probing the helical gap [26, 27]. Therefore, in the following we analyze results for a range of  $\alpha$  values. We take width of the wire  $W = 104$  nm [28]. In Fig. 2 a) we plot map of the decay length  $\xi$  in the topological phase  $E_z^2 > \Delta^2 + \tilde{\mu}^2$ . Due to rescaling of the chemical potential the contour of the topological regime in the diagram clearly deviates from the hyperbolic shape as recently measured for parallel orientation of the field [14]. Furthermore, in the map we observe strong dependence of  $\xi$  on the chemical potential absent in the case of negligible orbital effects of the magnetic field [32]. With the white curve we depict the topological transition without the SO-paramagnetic effects, which shows narrower range of  $B$  values for which the system is in topological regime.

Figure 2 b) with dashed curves shows the decay length for two strengths of the Rashba coupling without the orbital effects of the magnetic field. The increase of  $E_z$  in Eq. (10) leads to the enhancement of the decay length as presented in the figure. Interestingly, the inclusion of the diamagnetic and kinetic-paramagnetic effects (dot-dashed curves) leads to the strong suppression of the decay length, up to a factor of three for the case of the strong SO coupling  $\alpha = 50$  meVnm depicted with the red curve. The detrimental effect on the decay length reduction through the SO-paramagnetic effects are manifested by the solid curves that approach the ones obtained with the sole Zeeman splitting. Note however that for the both considered Rashba strengths,  $\xi$  still remains lower with the orbital magnetic effects included as compared to the case of the Zeeman splitting only.

*Beyond low-energy approximation.* The above consideration focused on the band mixing limited only to the two lowest-energy transverse subbands. For stronger magnetic field or SO coupling this approach must unavoidably break. Furthermore the validity of decay lengths obtained through Eq. (10) is limited to small  $k_x$  and  $\alpha$  [30]. Now we turn our attention to exact solution of the Hamiltonian (1) to test the validity of the developed theory and to extend our study beyond the above mentioned limits. For this purpose, we diagonalize numerically the Hamiltonian (1) on a square mesh with  $\Delta x = \Delta y = 4$  nm. The orbital effects of the magnetic field are incorporated using Peierls substitution of hopping elements  $t_{nm} \rightarrow t_{nm} \exp[-ie \int \mathbf{A} d\mathbf{l}/\hbar]$ . In Fig. 1 b) with the black crosses we depict the dispersion relation obtained from the numerical calculations. As we see the agreement between the analytical and the numerical results is exceptionally good.

Finally we complement the study with numerical assessment of the decay lengths. The spatial extent of MBSs is obtained numerically as the largest decay length  $\xi = \max \text{Re}[\kappa]^{-1}$  of the evanescent waves  $\Psi \sim e^{-\kappa x}$  at zero energy, with  $\kappa$  being the eigenvalue of the translational operator [32]. We perform eigendecomposition of the translation operator for a infinite wire described by

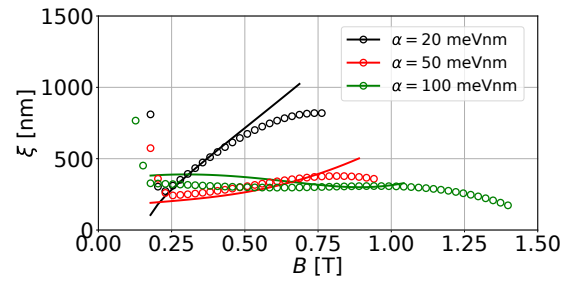


Figure 3. Majorana bound state decay length  $\xi$  as a function of the magnetic field for three values of the Rashba coupling strength. Solid curves correspond to the analytical model of Eq. (10) while open circles are results of the exact numerical diagonalization of Hamiltonian (1). Results for  $\alpha = 20, 50$  meVnm correspond to those on Fig. 2 b) and the data for  $\alpha = 100$  meVnm is obtained for  $\mu = 1.57$  meV.

the Hamiltonian (1). The topological transition is determined from the change of the topological invariant calculated as the determinant of the reflection matrix  $\text{sgn}(\det[R])$  of a finite slice of the wire contacted with normal and superconducting electrodes [33]. All calculations are performed in Kwant package [34].

Figure 3 with open circles presents numerical results for the decay lengths. We observe great agreement with the developed theory that persist up to the topological phase closing, where the increasing magnetic field and wave-vector breaks the applicability of both the two-band model and validity of the formula given by Eq. (10). Interestingly, in this regime, in the exact calculation we observe further beneficial reduction of the decay length which leads to decreasing amplitude of the energy oscillation of the overlapping MBSs [28].

Summarizing, we studied impact of the orbital effects of the perpendicular magnetic field on the decay length of the Majorana bound states in the proximitized semiconductor wire. We provided quasi-one-dimensional analytical model that allows to quantify the energies and decay lengths of Majorana modes in the low-density limit, which we validated by comparison with exact numerical calculations. We found that the reduction of the decay length via diamagnetic rescaling of the chemical potential is assisted by the change of the effective mass due to subband mixing by the paramagnetic term in the kinetic energy operator. On the other hand, the vector potential entering through the SO coupling Hamiltonian has rudimentary effect on the decay length reduction by the enhancement of the chemical potential and the decrease of the Rashba coupling constant. We found however, that in total, the spatial extent of the Majorana modes is still less than without the orbital magnetic effects in favor of the topological robustness of Majorana states in finite size quantum gate devices on composite nanowires [7–9].

This work was supported by National Science Centre (NCN) agreement number UMO-2016/23/D/ST3/00394

and partially by PL-Grid Infrastructure.

- 
- [1] Y. Oreg, G. Refael, and F. von Oppen, *Phys. Rev. Lett.* **105**, 177002 (2010).
- [2] J. D. Sau, R. M. Lutchyn, S. Tewari, and S. Das Sarma, *Phys. Rev. Lett.* **104**, 040502 (2010).
- [3] A. Y. Kitaev, *Annals of Physics* **303**, 2 (2003).
- [4] J. Alicea, Y. Oreg, G. Refael, F. v. Oppen, and M. P. A. Fisher, *Nat. Phys.* **7**, 412 (2011).
- [5] B. v. Heck, A. R. Akhmerov, F. Hassler, M. Burrello, and C. W. J. Beenakker, *New J. Phys.* **14**, 035019 (2012).
- [6] T. Hyart, B. van Heck, I. C. Fulga, M. Burrello, A. R. Akhmerov, and C. W. J. Beenakker, *Phys. Rev. B* **88**, 035121 (2013).
- [7] S. R. Plissard, I. van Weperen, D. Car, M. A. Verheijen, G. W. G. Immink, J. Kammhuber, L. J. Cornelissen, D. B. Szombati, A. Geresdi, S. M. Frolov, L. P. Kouwenhoven, and E. P. A. M. Bakkers, *Nat. Nano.* **8**, 859 (2013).
- [8] E. M. T. Fadaly, H. Zhang, S. Conesa-Boj, D. Car, Ö. Gül, S. R. Plissard, R. L. M. Op het Veld, S. Kölling, L. P. Kouwenhoven, and E. P. A. M. Bakkers, *Nano Lett.* **17**, 6511 (2017).
- [9] S. Gazibegovic, D. Car, H. Zhang, S. C. Balk, J. A. Logan, M. W. A. de Moor, M. C. Cassidy, R. Schmits, D. Xu, G. Wang, P. Krogstrup, R. L. M. Op het Veld, K. Zuo, Y. Vos, J. Shen, D. Bouman, B. Shojaei, D. Pennachio, J. S. Lee, P. J. van Veldhoven, S. Koelling, M. A. Verheijen, L. P. Kouwenhoven, C. J. Palmstrøm, and E. P. A. M. Bakkers, *Nature* **548**, 434 (2017).
- [10] V. Mourik, K. Zuo, S. M. Frolov, S. R. Plissard, E. P. a. M. Bakkers, and L. P. Kouwenhoven, *Science* **336**, 1003 (2012).
- [11] M. T. Deng, C. L. Yu, G. Y. Huang, M. Larsson, P. Caroff, and H. Q. Xu, *Nano Lett.* **12**, 6414 (2012).
- [12] A. D. K. Finck, D. J. Van Harlingen, P. K. Mohseni, K. Jung, and X. Li, *Phys. Rev. Lett.* **110**, 126406 (2013).
- [13] H. O. H. Churchill, V. Fatemi, K. Grove-Rasmussen, M. T. Deng, P. Caroff, H. Q. Xu, and C. M. Marcus, *Phys. Rev. B* **87**, 241401 (2013).
- [14] J. Chen, P. Yu, J. Stenger, M. Hoeser, D. Car, S. R. Plissard, E. P. A. M. Bakkers, T. D. Stanescu, and S. M. Frolov, *Sci. Adv.* **3**, e1701476 (2017).
- [15] J. Shabani, M. Kjaergaard, H. J. Suominen, Y. Kim, F. Nichele, K. Pakrouski, T. Stankevic, R. M. Lutchyn, P. Krogstrup, R. Feidenhans'l, S. Kraemer, C. Nayak, M. Troyer, C. M. Marcus, and C. J. Palmstrøm, *Phys. Rev. B* **93**, 155402 (2016).
- [16] P. Krogstrup, N. L. B. Ziino, W. Chang, S. M. Albrecht, M. H. Madsen, E. Johnson, J. Nygård, C. M. Marcus, and T. S. Jespersen, *Nat. Mater.* **14**, 400 (2015).
- [17] M. Kjaergaard, H. J. Suominen, M. P. Nowak, A. R. Akhmerov, J. Shabani, C. J. Palmstrøm, F. Nichele, and C. M. Marcus, *Phys. Rev. Applied* **7**, 034029 (2017).
- [18] W. Chang, S. M. Albrecht, T. S. Jespersen, F. Kuemmeth, P. Krogstrup, J. Nygård, and C. M. Marcus, *Nat. Nano.* **10**, 232 (2015).
- [19] M. Kjaergaard, F. Nichele, H. J. Suominen, M. P. Nowak, M. Wimmer, A. R. Akhmerov, J. A. Folk, K. Flensberg, J. Shabani, C. J. Palmstrøm, and C. M. Marcus, *Nat. Commun.* **7**, 12841 (2016).
- [20] H. Zhang, C.-X. Liu, S. Gazibegovic, D. Xu, J. A. Logan, G. Wang, N. van Loo, J. D. S. Bommer, M. W. A. de Moor, D. Car, R. L. M. O. h. Veld, P. J. van Veldhoven, S. Koelling, M. A. Verheijen, M. Pendharkar, D. J. Pennachio, B. Shojaei, J. S. Lee, C. J. Palmstrom, E. P. A. M. Bakkers, S. D. Sarma, and L. P. Kouwenhoven, *arXiv:1710.10701* (2017).
- [21] J. S. Lim, L. Serra, R. López, and R. Aguado, *Phys. Rev. B* **86**, 121103 (2012).
- [22] J. Osa and L. Serra, *Phys. Rev. B* **91**, 235417 (2015).
- [23] B. Nijholt and A. R. Akhmerov, *Phys. Rev. B* **93**, 235434 (2016).
- [24] O. Dmytruk and J. Klinovaja, *arXiv:1710.01671* (2017).
- [25] I. van Weperen, B. Tarasinski, D. Eeltink, V. S. Pribiag, S. R. Plissard, E. P. A. M. Bakkers, L. P. Kouwenhoven, and M. Wimmer, *Phys. Rev. B* **91**, 201413 (2015).
- [26] S. Heedt, N. T. Ziani, F. Crépin, W. Prost, S. Trelenkamp, J. Schubert, D. Grützmacher, B. Trauzettel, and T. Schäpers, *Nat. Phys.* **13**, 563 (2017).
- [27] J. Kammhuber, M. C. Cassidy, F. Pei, M. P. Nowak, A. Vuik, Ö. Gül, D. Car, S. R. Plissard, E. P. a. M. Bakkers, M. Wimmer, and L. P. Kouwenhoven, *Nat. Commun.* **8**, 478 (2017).
- [28] See the Supplemental Materials.
- [29] S. D. Sarma, M. Freedman, and C. Nayak, *npj Quantum Information* **1**, 15001 (2015).
- [30] S. Das Sarma, J. D. Sau, and T. D. Stanescu, *Phys. Rev. B* **86**, 220506 (2012).
- [31] S. Nadj-Perge, V. S. Pribiag, J. W. G. van den Berg, K. Zuo, S. R. Plissard, E. P. A. M. Bakkers, S. M. Frolov, and L. P. Kouwenhoven, *Phys. Rev. Lett.* **108**, 166801 (2012).
- [32] D. Sticlet, B. Nijholt, and A. Akhmerov, *Phys. Rev. B* **95**, 115421 (2017).
- [33] I. C. Fulga, F. Hassler, A. R. Akhmerov, and C. W. J. Beenakker, *Phys. Rev. B* **83**, 155429 (2011).
- [34] C. W. Groth, M. Wimmer, A. R. Akhmerov, and X. Waintal, *New J. Phys.* **16**, 063065 (2014).